# A Powerful, Line-of-Sight AGN Outburst in RBS 797

K. W. CAVAGNOLO[1,2], B. R. MCNAMARA[1,3,4], M. W. WISE[5],
P. E. J. NULSEN[4], M. BRÜGGEN[6], M. GITTI[4,7], AND D. A. RAFFERTY[8]

*Draft version November 23, 2010*

## ABSTRACT

Utilizing a $\sim 40$ ks observation from the Chandra X-ray Observatory, we present spatially resolved analysis of the intracluster medium, cavities, and the nuclear point source of RBS 797.

*Subject headings:*

## 1. INTRODUCTION

Evidence has amassed over the last decade that the growth of galaxies and supermassive black holes (SMBHs) are coupled, and that energetic feedback from active galactic nuclei (AGN) strongly influences galaxy evolution (*e.g.* Kormendy & Richstone 1995; Magorrian et al. 1998; Silk & Rees 1998; Kauffmann & Haehnelt 2000; Ferrarese & Merritt 2000; Gebhardt et al. 2000; Tremaine et al. 2002). The discovery of AGN induced cavities in the hot halos surrounding many massive galaxies has strengthened this theory (see McNamara & Nulsen 2007, for a review), revealing that AGN mechanical heating is capable of regulating the radiative cooling responsible for late-time galaxy growth (*e.g.* Bîrzan et al. 2004; Dunn & Fabian 2006; Rafferty et al. 2006). Current models of this late-time feedback loop posit that cooling processes in a galaxy's halo result in mass accretion onto a central SMBH, thereby driving AGN activity and ultimately heating the cooling halo (*e.g.* Croton et al. 2006; Bower et al. 2006; Sijacki et al. 2007). While there is direct evidence that halo cooling and feedback are linked (*e.g.* Cavagnolo et al. 2008a; Rafferty et al. 2008), the observational constraints on how AGN are fueled and powered remain loose. For example, what fraction of the energy released in an AGN outburst is attributable to the gravitational binding energy of accreting matter and a SMBH's rotational energy is still unclear (see Begelman et al. 1984 and Meier 2002 for reviews).

Mass accretion alone can, in principle, fuel most AGN (*e.g.* Pizzolato & Soker 2005; Allen et al. 2006), and is typically not at odds with the gas masses and stellar masses of the host galaxy (*e.g.* Rafferty et al. 2006). However, there are systems which are gas-poor and host very powerful AGN where mass accretion alone does not appear to be capable of sustaining the outburst. For example, in the galaxy clusters Hercules A, Hydra A, MS 0735.6+7421, and RBS 797(the focus of this paper), an AGN in each cluster's brightest cluster galaxy (BCG) has deposited of the order $10^{61}$ erg of energy into the surrounding intracluster medium (ICM) at rates around $10^{45}$ erg s$^{-1}$ (Nulsen et al. 2005; Wise et al. 2007; McNamara et al. 2005). The importance of these systems for understanding AGN feedback is that the fueling appears to have been astoundingly efficient, which has led to speculation that some BCGs may host an ultramassive black hole ($> 10^{10}$ M$_\odot$; *e.g.* McNamara et al. 2009), or that some outbursts are primarily powered by the release of energy stored in a rapidly spinning SMBH (*e.g.* McNamara et al. 2010). As additional extremely energetic AGN outbursts are found, it may be necessary to reconsider just how massive SMBHs can become, or incorporate alternate feedback pathways, like spin, into galaxy formation models (*e.g.* Hughes & Blandford 2003; Sikora et al. 2007; Benson & Babul 2009).

The discovery of ICM cavities in RBS 797 was first reported by Schindler et al. (2001) using data from the Chandra X-ray Observatory (*CXO*). Multifrequency radio observations showed that the cavities are co-spatial with extended radio emission centered on a strong, jetted radio source coincident with the RBS 797 BCG (De Filippis et al. 2002; Gitti et al. 2006; Bîrzan et al. 2008). The observations implicate an AGN in the BCG as the cavities' progenitor, and Bîrzan et al. (2004, hereafter B04) estimate the AGN deposited $\approx 10^{60}$ erg of energy into the ICM at a rate of $\approx 10^{45}$ erg s$^{-1}$. The B04 analysis assumed the cavities are roughly spherical, symmetric about the plane of the sky, and that their centers lie in a plane passing through the central AGN and perpendicular to our line-of-sight. However, the abnormally deep surface brightness decrements of the cavities, and the nebulous correlation between the radio and X-ray morphologies, suggests the system may be more complex than B04 could constrain. Using a longer, follow-up *CXO* observation, we determine that the cavities are indeed elongated along the line-of-sight, and go on to provide evidence that additional cavities may be present at larger radii. We conservatively estimate the total AGN energy output and power are six times larger than the B04 values, $\approx 6 \times 10^{60}$ erg and $\approx 6 \times 10^{45}$ erg s$^{-1}$ respectively, and discuss whether mass accretion alone could have powered such an outburst.

Reduction of X-ray and radio data is discussed in Section 2. Interpretation of observational results are given throughout Section 3, and a brief summary concludes the paper in Section 4. A $\Lambda$CDM cosmology with $H_0 = 70$ km s$^{-1}$ Mpc$^{-1}$, $\Omega_M = 0.27$, and $\Omega_\Lambda = 0.73$ is adopted. At a redshift of $z = 0.354$, the look-back time is 3.9 Gyr, $D_A = 4.996$ kpc arcsec$^{-1}$, and

[1] University of Waterloo, 200 University Ave. W., Waterloo, ON, N2L 3G1, Canada.
[2] UNS, CNRS UMR 6202 Cassiopée, Observatoire de la Côte d'Azur, Nice, France.
[3] Perimeter Institute for Theoretical Physics, 31 Caroline St. N., Waterloo, ON, N2L 2Y5, Canada.
[4] Harvard-Smithsonian Center for Astrophysics, 60 Garden St, Cambridge, MA, 02138-1516, United States.
[5] Astronomical Institute Anton Pannekoek, P.O. Box 94249, 1090 GE Amsterdam, The Netherlands.
[6] Jacobs University Bremen, P.O. Box 750561, 28725 Bremen, Germany.
[7] INAF-Astronomical Observatory of Bologna, Via Ranzani 1, I-40127 Bologna, Italy.
[8] Leiden Observatory, University of Leiden, P.O. 9513, 2300 RA Leiden, The Netherlands.

$D_L$ = 1889 Mpc. All errors are 68% confidence unless stated otherwise.

## 2. OBSERVATIONS

### 2.1. *X-ray Data*

RBS 797 was observed with *CXO* in October 2000 for 11.4 ks using the ACIS-I array (ObsID 2202) and in July 2007 for 38.3 ks using the ACIS-S array (ObsID 7902). Datasets were reduced using CIAO and CALDB versions 4.2. Events were screened of cosmic rays using *ASCA* grades and VFAINT filtering. The level-1 events files were reprocessed to apply the most up-to-date corrections for the time-dependent gain change, charge transfer inefficiency, and degraded quantum efficiency of the ACIS detector. The afterglow and dead area corrections were also applied. Time intervals affected by background flares exceeding 20% of the mean background count rate were isolated and removed using light curve filtering. The final, combined exposure time is 48.8 ks. Point sources were identified and removed via visual inspection and use of the CIAO tool WAVDETECT. We refer to the *CXO* data free of point sources and flares as the "clean" data. A mosaiced, fluxed image (see Figure 1) was generated by exposure correcting each clean dataset and reprojecting the normalized images to a common tangent point.

### 2.2. *Radio Data*

Very Large Array (*VLA*) radio images at 325 MHz (A-array), 1.4 GHz (A- and B-array), 4.8 GHz (A-array), and 8.4 GHz (D-array) are presented in Gitti et al. (2006) and Bîrzan et al. (2008). Our re-analysis of the archival *VLA* radio observations yielded no significant differences with these prior studies. Using the rms noise ($\sigma_{rms}$) values given in Gitti et al. (2006) and Bîrzan et al. (2008) for each observation, emission contours between $3\sigma_{rms}$ and the peak image intensity were generated. These are the contours referenced and shown in all subsequent discussion and figures.

## 3. RESULTS

### 3.1. *Cavity Morphologies and ICM Substructure*

Shown in Figure 1 is the 0.7–2.0 keV *CXO* mosaiced clean image and an *HST* optical image of the RBS 797 BCG. Outside of ≈ 50 kpc, the global ICM morphology is regular and elliptical in shape, with the appearance of being skewed along the northwest-southeast direction. The cavities discovered by Schindler et al. (2001) are clearly seen in the cluster core east and west of the nuclear X-ray source and appear to be enclosed by a thick, bright, elliptical ridge of emission which we discuss further in Section 3.3.1. The western cavity has more internal structure, and its boundaries are less well-defined, than the eastern cavity. The emission from the innermost region of the core is elongated north-south and has a distinct shape punctuated by a hard nuclear X-ray source. Comparison of the *HST* optical and *CXO* X-ray images reveals the BCG coincides with the nuclear X-ray source and has the appearance of being pinched into two equal brightness halves. It is unclear which, if either, is at the center of the galaxy or might be associated with an AGN. There is substantial structure to the BCG optical halo, and its association with the AGN is discussed in Section 3.6.

Multifrequency radio images overlaid with ICM X-ray contours are shown in Figure 2. RBS 797 radio properties are discussed in Gitti et al. (2006), and we summarize here. As seen in projection, the nuclear 4.8 GHz jets are almost orthogonal to the axis connecting the cavities. The 325 MHz, 1.4 GHz, and 8.4 GHz radio emission are diffuse and extend well-beyond the cavities, more similar to the morphology of a radio mini-halo than relativistic plasma confined to the cavities (Doria et al., in preparation). Of all the radio images, the 1.4 GHz emission most closely traces the cavity morphologies, yet it is still diffuse and uniform over the cavities with little structure outside the radio core. Typically, the connection between a cavity system, coincident radio emission, and the progenitor AGN is unambiguous. This is not the case for RBS 797, which suggests the cavity system may be more complex than it appears.

To better reveal the cavity morphologies, residual X-ray images of RBS 797 were constructed by modeling the ICM emission and subtracting it off. The X-ray isophotes of two exposure-corrected images – one smoothed by a 1″ Gaussian and another by a 3″ Gaussian – were fitted with ellipses using the IRAF task ELLIPSE. The ellipse centers were fixed at the location of the BCG X-ray point source, and the eccentricities and position angles were free to vary. A 2D surface brightness model was created from each fit using the IRAF task BMODEL, normalized to the parent X-ray image, and then subtracted off. The residual images are shown in Figure 3.

In addition to the central east and west cavities (labeled E1 and W1), depressions north and south of the nucleus (labeled N1 and S1) are revealed. N1 and S1 lie along the 4.8 GHz jet axis and are coincident with spurs of significant 1.4 GHz emission, indicating they may be related to activity of the central AGN. A depression coincident with the southeastern concentration of 325 MHz emission is also found (labeled E2), but no counterpart on the opposing side of the cluster is seen (labeled W2). There is an X-ray edge which extends southeast from E2 and sits along a ridge of 325 MHz and 8.4 GHz emission. No substructure associated with the western-most knot of 325 MHz emission is found, but there is a stellar object co-spatial with this region. The X-ray and radio properties of the object are consistent with those of a galactic RS CVn star (Seaquist 1993) – if the star is less than 1 kpc away, $L_X \lesssim 10^{31}$ erg s$^{-1}$ and $L_{325} \sim 10^{27}$ erg s$^{-1}$ – suggesting the western 325 MHz emission may not be associated with the cluster.

### 3.2. *Radial ICM Properties*

In order to analyze the RBS 797 cavity system and AGN outburst energetics in-detail, the radial ICM density, temperature, and pressure structure need to be quantified. The radial profiles discussed below are shown in Figure 4. A temperature ($kT_X$) profile was created by extracting spectra from concentric circular annuli (2500 source counts per annulus) centered on the cluster X-ray peak, binning the spectra to 25 counts per energy channel, and then fitting each spectrum in XSPEC 12.4 (Arnaud 1996) with an absorbed, single-component MEKAL model (Mewe et al. 1985) over the energy range 0.7–7.0 keV. For each annulus, weighted responses were created and a background spectrum was extracted from the ObsID matched CALDB blank-sky dataset normalized using the ratio of 9–12 keV count rates for an identical off-axis, source-free region of the blank-sky and target datasets. The absorbing Galactic column density was fixed to $N_{H,Gal} = 2.28 \times 10^{20}$ cm$^{-2}$ (Kalberla et al. 2005), and a spectral model for the Galactic foreground was included as an additional, fixed background component during spectral fit-

ting (see Vikhlinin et al. 2005 and Cavagnolo et al. 2008b for method). Gas metal abundance was free to vary and normalized to the Anders & Grevesse (1989) solar ratios. Spectral deprojection using the PROJ XSPEC model did not produce significantly different results, thus only projected quantities are discussed.

A 0.7–2.0 keV surface brightness profile was extracted from the *CXO* mosaiced clean image using concentric $1''$ wide elliptical annuli centered on the BCG X-ray point source (central $\approx 1''$ and cavities excluded). A deprojected electron density ($n_e$) profile was derived from the surface brightness profile using the method of Kriss et al. (1983) which incorporates the 0.7–2.0 keV count rates and best-fit normalizations from the spectral analysis (see Cavagnolo et al. 2009, for details). Errors for the density profile were estimated using 5000 Monte Carlo simulations of the original surface brightness profile. A total gas pressure profile was calculated as $P = nkT_X$ where $n \approx 2.3n_H$ and $n_H \approx n_e/1.2$. Profiles of enclosed X-ray luminosity, entropy ($K = kT_X n_e^{-2/3}$) and cooling time ($t_{cool} = 3nkT_X (2n_e n_H \Lambda)^{-1}$, where $\Lambda$ is the cooling function), were also generated. Errors for each profile were determined by summing the individual parameter uncertainties in quadrature.

### 3.3. *ICM Cavities*

#### 3.3.1. *Energetics*

Of all the ICM substructure, the E1 and W1 cavities are unambiguous detections, and their energetics were determined following standard methods (see B04). Our fiducial cavity configuration assumes the cavities are symmetric about the plane of the sky, and the cavity centers lie in a plane which is perpendicular to our line-of-sight and passes through the central AGN (configuration-1 in Figure 5). Hereafter, we denote the line-of-sight distance of a cavity's center from this plane as $z$, and the cavity radius along the line-of-sight as $r_{los}$. The volume of a cavity is thus $V = 4\pi ab r_{los}/3$ where $a$ and $b$ are the projected semi-major and -minor axes, respectively, of the by-eye determined ellipses in Figure 3. The projected morphologies of E1 and W1 are similar enough that the same regions were used for both. Initially, the cavities were assumed to be roughly spherical and $r_{los}$ was set equal to the projected effective radius, $r_{eff} = \sqrt{ab}$. For configuration-1, the distance of each cavity from the central AGN, $D$, is simply the projected distance from the ellipse centers to the BCG X-ray point source. A systematic error of 10% is assigned to the cavity volumes.

Cavity ages were estimated using the three time scales discussed in B04: ICM sound speed age ($t_{sonic}$), buoyant rise time age ($t_{buoy}$), and volume refilling age ($t_{refill}$). The energy in each cavity, $E_{cav} = \gamma PV/(\gamma - 1)$, was calculated assuming the contents are a relativistic plasma ($\gamma = 4/3$), and that the mean internal cavity pressure is equal to the ICM pressure at the cavity mid-point. We assume the cavities are detached, buoyant structures and that the time-averaged energy needed to create each cavity is $P_{cav} = E_{cav}/t_{buoy}$. The individual cavity properties are given in Table 1 and the aggregate properties in Table 2.

For the spherical assumption of configuration-1, we measure a total cavity energy $E_{cav} = 3.23\ (\pm 1.16) \times 10^{60}$ erg and total power $P_{cav} = 3.34\ (\pm 1.41) \times 10^{45}$ erg s$^{-1}$. These values are larger than those of B04 ($E_{cav} = 1.52 \times 10^{60}$ erg, $P_{cav} = 1.13 \times 10^{44}$ erg s$^{-1}$) by a factor of $\approx 3$ as a result of our

larger E1 and W1 volumes. Using the B04 cavity volumes in place of our own produces no significant differences between our energetics calculations and those of B04. The largest uncertainties in the energetic calculations are the cavity volumes and their 3-dimensional locations in the ICM, issues we consider next.

#### 3.3.2. *Decrements*

A cavity's morphology and location in the ICM dictates the X-ray surface brightness decrement it induces. If the surface brightness of the undisturbed ICM can be estimated, then the decrement is useful for constraining the cavity line-of-sight size and its distance from the launch point (*i.e.* $r_{los}$ and $z$, respectively; see Wise et al. 2007, for details). We define surface brightness decrement, $y$, as the ratio of the X-ray surface brightness inside the cavities to the value of the best-fit ICM surface brightness $\beta$-model at the same radius. Consistent with the analysis of Schindler et al. (2001), we find the best-fit $\beta$-model has parameters $S_0 = 1.65\ (\pm 0.15) \times 10^{-3}$ ct s$^{-1}$ arcsec$^{-2}$, $\beta = 0.62 \pm 0.04$, and $r_{core} = 7.98'' \pm 0.08$ for $\chi^2$(DOF) = 79(97). Using a circular aperture with radius $1''$ centered on the deepest part of each cavity, we measure mean decrements of $\bar{y}_{W1} = 0.50 \pm 0.18$ and $\bar{y}_{E1} = 0.52 \pm 0.23$, with minima of $y_{W1}^{min} = 0.44$ and $y_{E1}^{min} = 0.47$.

To check if the spherical approximation for cavity configuration-1 can produce the measured decrements, the best-fit $\beta$-model was integrated over each cavity with a column of gas equal to $2r_{los}$ excluded. The integration revealed decrements less than 0.6 cannot be achieved for the spherical case, indicating our assumption of $r_{los} = r_{eff}$ is poor. If the centers of E1 and W1 lie in the plane of the sky, the minimum line-of-sight depths needed to reproduce the decrements of E1 and W1 are $r_{los}^{E1} = 23.35$ kpc and $r_{los}^{W1} = 25.96$ kpc. The energetics for these morphologies are given as configuration-1a in Tables 1 and 2. If the cavities are moving away from the AGN along an axis perpendicular to our line-of-sight, then it is a bit odd that the cavities are compressed in the orthogonal direction. But, it may be that the cavities are larger along that axis than we realize, for example if the bright rims are masking the true extent of the cavities. It is also possible that the cavities are inflating close to our line-of-sight and thus may be large, elongated structures as shown in configuration-2 of Figure 5.

Presented in Figure 6 are curves showing how surface brightness decrement changes as a function of $z$ for various $r_{los}$. The plots demonstrate that it is possible to reproduce the measured E1 and W1 decrements using larger cavities that have centers displaced from the plane of the sky. Consequently, the limiting case of $z = 0$ is a lower-limit on the AGN outburst energetics. If the cavity system lies close to our line-of-sight, and is much larger and more complex than the data allows us to constrain, it may explain the additional ICM substructures seen in the residual images and the ambiguous relationship between the X-ray and radio morphologies.

It should be noted that deep cavities like in RBS 797 are uncommon, with most other cavity systems having minima greater than 0.6 (B04). The extreme decrements raise the concern that the $\beta$-model fit has been influenced by the rim-like structures of E1-W1 and produced artificially low decrements. The prominent rims can be seen in Figure 7 which shows the normalized surface brightness variation in wedges of a $2.5''$ wide annulus centered on the X-ray peak and passing through the cavity midpoints. In addition to excluding the cavities, we tried excluding the rims during $\beta$-model fitting, but this did

not provide insight as too much of the surface brightness profile was removed and the fit did not converge. Extrapolating the surface brightness profile at larger radii inward resulted in even lower decrements. The rims, and their possible connection to gas shocking, are discussed below.

### 3.3.3. *Do the Rims Indicate Shocks?*

It is often assumed that cavity energetics calculations, like those in Section 3.3.1, provide a reasonable estimate of the physical quantity jet power, $P_{\rm jet}$. However, $P_{\rm cav}$ and $P_{\rm jet}$ do not account for AGN output energy which may be channeled into shocks. Though the *CXO* data does not indicate the presence of significant density or temperature jumps – which would confirm the presence of a shock – the cavity/rim morphologies and energetics are strikingly similar to those of MS 0735.6+7421, which hosts a large-scale Mach $\approx 1.4$ shock. If significant ICM shocking has occurred in RBS 797, then the cavity energetics clearly underestimate the AGN output, which directly impacts the discussion of AGN fueling in Section 3.4.

A simplistic model that captures how a bright, shocked rim helps enhance a cavity decrement is to assume the shocked region is cylindrical and uniformly compressed. Ignoring emission outside the shocked cylinder, a compression $\chi$ gives a decrement $y = 1 + \sqrt{\chi - 1} - \sqrt{\chi}$, hence a decrement of $\approx 50\%$ can be obtained with $\chi \approx 1.56$, *i.e.* comparable to a Mach 1.4 shock like in MS 0735.6+7421. This is a rough estimate (arguably pessimistic), but it demonstrates that we may be seeing shocking in RBS 797. Assuming axial symmetry for the unshocked gas, including emission outside the cylinder adds more to the bright rim than the cavity center, increasing the surface brightness difference from rim to "cavity," but also reducing the decrement. Because the ICM surface brightness drops rapidly outside the shocked region, the correction is modest, and it scales as $\chi^{-3/2}$, so its effect decreases as the compression increases.

### 3.4. *Powering the Outburst*

If the AGN was powered by mass accretion alone, then $E_{\rm cav}$ is representative of the gravitational binding energy released as mass accreted onto the SMBH. In which case, the total mass accreted can be approximated as $M_{\rm acc} = E_{\rm cav}/(\epsilon c^2)$ with an average accretion rate $\dot{M}_{\rm acc} = M_{\rm acc}/t_{\rm buoy}$. Consequently, the black hole's mass grew by $\Delta M_{\rm BH} = (1 - \epsilon)M_{\rm acc}$ at an average rate $\dot{M}_{\rm BH} = \Delta M_{\rm BH}/t_{\rm buoy}$. Here, $\epsilon$ is a poorly understood mass-energy conversion factor which may vary from 0.06–0.40, and we adopt the commonly used 0.1 (Frank et al. 2002). The accretion properties associated with each cavity configuration are given in Table 2, and below we consider if the accretion of cold or hot gas pervading the BCG could meet these requirements without being in conflict with observed BCG and ICM properties.

### 3.4.1. *Cold Accretion*

Substantial quantities of cold molecular gas and optical nebulae are found in many cool core clusters (Crawford et al. 1999; Edge 2001). If rapidly cooling thermal instabilities form in these structures, it is possible that they are the source of fuel for AGN activity and star formation (*e.g.* Pizzolato & Soker 2005, 2010). The molecular gas mass ($M_{\rm mol}$) of RBS 797 has not been measured, so it was inferred using the $M_{\rm mol}$-H$\alpha$ correlation in Edge (2001). An optical spectrum (3200-7600 Å) of the RBS 797 BCG reveals a strong

H$\beta$ emission line (Fischer et al. 1998; Schwope et al. 2000), which we used as a surrogate for H$\alpha$ by assuming a Balmer decrement of EW$_{{\rm H}\beta}$/EW$_{{\rm H}\alpha}$ = 0.29 (Moustakas et al. 2006), where EW is line equivalent width. Under these assumptions, we estimate $M_{\rm mol} \sim 10^{10}$ M$_\odot$, sufficiently in excess of the $\sim 10^7$ M$_\odot$ needed to power the outburst that we can infer there is an ample cold gas reservoir capable of providing fuel. It must be noted that the $M_{\rm mol}$-H$\alpha$ relation has substantial scatter (Salomé & Combes 2003), and that the RBS 797 emission line measurements are highly uncertain (A. Schwope, private communication), so the $M_{\rm mol}$ estimate is simply informative.

Accreting gas from the reservoir will cause the central SMBH mass to grow, but black hole mass growth is also coupled to the star formation properties of the host galaxy (*e.g.* Kormendy & Richstone 1995; Ferrarese & Merritt 2000). The Magorrian relation (Magorrian et al. 1998) tells us that for each unit of black hole mass growth, several hundred times as much goes into bulge stars (*e.g.* Häring & Rix 2004). Thus, the $\sim 1$ M$_\odot$ yr$^{-1}$ mass accretion rate needed to power the RBS 797 outburst requires that $\sim 100$ M$_\odot$ yr$^{-1}$ of star formation needed to accompany the AGN fueling event. If we assume the present BCG star formation rate (SFR), $\sim 1$–$10$ M$_\odot$ yr$^{-1}$ (see Section 3.6), is of the order the SFR preceding and during the AGN outburst, we encounter the awkward situation where every mass unit accreted by the SMBH resulted in a nearly equal amount of star formation, in conflict with expectations of SMBH-host galaxy co-evolution. Further, the RBS 797 BCG stellar halo color profile is inconsistent with high levels of recent star formation (see Section 3.6). This result comes with the caveat that $M_{\rm BH}$-SFR scaling relations may not hold at BCG mass scales. Given the limitations of the available data, it appears if cold accretion did power the outburst, it did so with incredible efficiency.

### 3.4.2. *Hot Accretion*

Direct accretion of the hot ICM via the Bondi mechanism provides another possible AGN fuel source. The accretion flow arising from this process is characterized by the Bondi equation (Equation 1) and is often compared with the Eddington limit describing the maximal accretion rate for a SMBH (Equation 2):

$$\dot{M}_{\rm Bon} = 0.013\, K_{\rm Bon}^{-3/2} \left( \frac{M_{\rm BH}}{10^9\, {\rm M}_\odot} \right)^2 {\rm M}_\odot\, {\rm yr}^{-1} \qquad (1)$$

$$\dot{M}_{\rm Edd} = \frac{2.2}{\epsilon} \left( \frac{M_{\rm BH}}{10^9\, {\rm M}_\odot} \right) {\rm M}_\odot\, {\rm yr}^{-1} \qquad (2)$$

where $\epsilon$ is a mass-energy conversion factor, $K_{\rm Bon}$ is the mean entropy [keV cm$^2$] of gas within the Bondi radius, and $M_{\rm BH}$ is black hole mass [M$_\odot$]. We chose the relations of Tremaine et al. (2002) and Graham (2007) to estimate $M_{\rm BH}$, and find a range of 0.6–7.8 $\times 10^9$ M$_\odot$, from which we adopted the weighted mean value $1.5^{+6.3}_{-0.9} \times 10^9$ M$_\odot$ where the errors span the lowest and highest $1\sigma$ values of the individual estimates. Fitting the ICM entropy profile with the function $K = K_0 + K_{100}(r/100\ {\rm kpc})^\alpha$, where $K_0$ [keV cm$^2$] is core entropy, $K_{100}$ [keV cm$^2$] is a normalization at 100 kpc, and $\alpha$ is a dimensionless index, reveals $K_0 = 17.9 \pm 2.2$ keV cm$^2$. For $\epsilon = 0.1$ and $K_{\rm Bon} = K_0$, the relevant accretion rates are $\dot{M}_{\rm Bon} \approx 4 \times 10^{-4}$ M$_\odot$ yr$^{-1}$ and $\dot{M}_{\rm Edd} \approx 33$ M$_\odot$ yr$^{-1}$. The Eddington and Bondi accretion ratios are given in Table 2, with $\dot{m}_{\rm E} \equiv \dot{M}_{\rm acc}/\dot{M}_{\rm Edd} \approx 0.02$ and $\dot{m}_{\rm B} \equiv \dot{M}_{\rm acc}/\dot{M}_{\rm Bon} \approx 2000$–$4000$.

The large value $\dot{m}_B$ is troublesome since it implies all the gas which reached the Bondi radius ($R_{\rm Bon} \approx 10$ pc) was accreted. But, $\dot{m}_B$ may be overestimated if $K_{\rm Bon} < K_0$ and $M_{\rm BH}$ is larger than our adopted value. Using the upper limit of $M_{\rm BH} \approx 8 \times 10^9$ M$_\odot$, and assuming gas near $R_{\rm Bon}$ has a mean temperature of 0.5 keV, a $\dot{m}_B$ of unity requires $K_{\rm Bon}$ be less than 1 keV cm$^2$, corresponding to $n_e \approx 0.4$ cm$^{-3}$. This is four times the measured ICM central density, and a sphere more than 2 kpc in radius is required for up to $10^7$ M$_\odot$ to be available for accretion. If the ICM is the source of the hot gas phase, these numbers imply the inner-core of the cluster is fully consumed during the outburst lifetime ($< 100$ Myr), which is much shorter than the central cooling time of the ICM ($\approx 400$ Myr), thereby short-circuiting the feedback loop.

Conversely, if the BCG harbors an ultramassive black hole, for example $> 10^{10}$ M$_\odot$, the strain on the Bondi mechanism is eased somewhat (*e.g.* McNamara et al. 2009). The optical surface brightness profile of the RBS 797 BCG does have a large core ($\approx 1.6$ kpc) which may indicate scouring by an ultramassive black hole. But, a "missing light" analysis (see McNamara et al. 2009) of the profile suggests a black hole mass of $\approx 6 \times 10^9$ M$_\odot$, within our existing estimates. While Bondi accretion cannot be ruled out because the nucleus is unresolved and the cluster is observed post-outburst when ICM core conditions may have dramatically changed, a number of observationally unsupported concessions need to be made for Bondi accretion to be viable.

### 3.4.3. *Black Hole Spin*

Powering the outburst by mass accretion alone appears to be inconsistent with the properties of the BCG and ICM. In an effort to find lower accretion rates which still produce powerful jets, we consider below if a rapidly-spinning SMBH could act as an alternate power source. We consider the spin model with the caveat that, like cold- and hot-mode accretion, spin is wrought with its own difficulties and is hard to evaluate for any one system (see McNamara et al. 2009 and McNamara et al. 2010 for discussion on these points).

In hybrid spin models (*e.g.* Meier 1999, 2001; Reynolds et al. 2006; Nemmen et al. 2007; Benson & Babul 2009; Garofalo et al. 2010) jets are produced by pairing the Blandford-Znajek (Blandford & Znajek 1977) and Blandford-Payne (Blandford & Payne 1982) mechanisms by extracting energy from a spinning black hole-accretion disk system via strong, wound magnetic fields. In these hybrid models, $\dot{m}_E$ dictates the black hole-accretion disk magnetic field strength needed to stabilize the system, which in turn determines the emergent jet power. Of the model parameters, only $P_{\rm jet}$ is truly measured, so a range of $\dot{m}_E$ and dimensionless spin values ($j$) can produce any particular $P_{\rm jet}$. However, to avoid the need for excessively large accretion rates, which is the shortcoming of pure mass accretion mechanisms, $j$ needs to be as near unity as possible, *i.e.* the choice of $\dot{m}_E$ is not completely arbitrary.

In the hybrid spin model of Nemmen et al. (2007), assuming an accretion disk viscosity of 0.25 (Quataert & Narayan 1999), the RBS 797 jet power can be reached for our fiducial values of $M_{\rm BH} = 1.5 \times 10^9$ M$_\odot$ and $\dot{m}_E = 0.02$ when $j > 0.96$, *i.e.* a near maximally spinning SMBH. However, the high accretion rate suffers from the same problems as cold- and hot- mode accretion. If $M_{\rm BH}$ has been underestimated and is larger than $3 \times 10^9$ M$_\odot$, for $j > 0.96$, accretion rates less than $0.01\dot{M}_{\rm Edd} \approx 0.3$ M$_\odot$ yr$^{-1}$ can achieve the RBS 797 jet power.

This is in good agreement with the argument presented in McNamara et al. (2010) which suggests for similarly powerful systems like MS 0735.6+7421 and Hercules A $\dot{m}_E$ cannot be much more than $\approx 0.02$. Additional relief can be found in the model of Garofalo et al. (2010) which has the feature that extremely powerful jets are produced for a SMBH which is spinning retrograde relative to the direction of the accreting material. In the Garofalo et al. (2010) model, for $\|j\| \geq 0.9$ and $M_{\rm BH} \geq 1.5 \times 10^9$ M$_\odot$, the required mass accretion rates are $\dot{m}_E \leq 0.005$ or $\lesssim 0.1$ M$_\odot$ yr$^{-1}$. So while the true value of $\dot{m}_E$ is unknown, there are reasonable accretion rates for a near maximally spinning SMBH which can reproduce the measured $P_{\rm jet}$ while not being in conflict with the BCG or ICM properties.

### *Nucleus Emission*

There is a bright BCG X-ray point source apparent in the *CXO* imaging, and its properties may also provide clues regarding past or ongoing accretion processes. A source spectrum was extracted from a region enclosing 90% of the normalized *CXO* PSF specific to the nuclear source median photon energy and off-axis position. The source region had an effective radius of $0.86''$, and a background spectrum was taken from an enclosing annulus that had 5 times the area. The shape and features of the background-subtracted spectrum, shown in Figure 8, are inconsistent with thermal emission so the spectrum was modeled using an absorbed power law with two Gaussians added to account for features which may be photoionized line blends. A variety of absorption models were fit to the spectrum, and the best-fit values are given in Table 3. The model with a power-law distribution of $N_{\rm H,obs} \sim 10^{22}$ cm$^{-2}$ absorbers yielded the best statistical fit, and the low column densities (well-below even moderately Compton-thick) indicate the nucleus is not heavily obscured.

If mass accretion is powering the nuclear emission, the X-ray source bolometric luminosity, $L_{\rm bol} = 2.21 \times 10^{44}$ erg s$^{-1}$, implies an accretion rate of $\dot{M}_{\rm acc} \approx L_{\rm bol}/(0.1c^2) \approx 0.04$ M$_\odot$ yr$^{-1}$ $\approx 0.001\dot{m}_E$. For this $\dot{M}_{\rm acc}$, the accretion disk model of Meier (2002) predicts an optical disk luminosity of $L_{\rm opt} \approx 8 \times 10^{44}$ erg s$^{-1}$, but no $L_{\rm opt} > 10^{44}$ erg s$^{-1}$ sources are found in the *HST* imaging and no optical point sources are found in the nucleus. The low column densities suggested by the X-ray modeling could not conceal such a source, so either the disk model is inappropriate for the nucleus, the optical emission is beamed away from us, or it is absent.

Extrapolation of the best-fit X-ray spectral model to radio frequencies reveals good agreement with the measured 1.4 GHz and 4.8 GHz nuclear radio fluxes. Further, the continuous injection synchrotron model of Heavens & Meisenheimer (1987) produced an acceptable fit to the X-ray, 1.4 GHz, and 4.8 GHz nuclear fluxes (see Figure 9). These results suggest the nuclear X-ray source may be synchrotron emission from unresolved jets (which are obvious in the high-resolution 4.8 GHz radio image), possibly with some contribution from low-level accretion. Regardless, there is no indication the X-ray source is the remnant of a very dense, hot gas phase which would be associated with an accretion event.

### 3.6. *AGN-BCG Interaction and Star Formation*

The RBS 797 BCG star formation properties are directly related to fueling of the AGN outburst through the Magorrian relation, and these properties were constrained using op-

tical and UV observations from the Hubble Space Telescope (*HST*), *GALEX*, and *XMM-Newton*/Optical Monitor (*XOM*). *HST* imaged RBS 797 using the ACS/WFC instrument and the F606W (4500–7500 Å; *V*) and F814W (6800–9800 Å; *I*) filters. Images produced by the Hubble Legacy Archive pipeline were used for analysis. There are two ACS artifacts in the *I* image which begin at $\approx 2.7''$ and $\approx 5.4''$ from the BCG center. Within a $2''$ aperture centered on the BCG, the measured magnitudes are $m_V = 19.3 \pm 0.7$ mag and $m_I = 18.2 \pm 0.6$ mag, consistent with non-*HST* measurements of Fischer et al. (1998), indicating the *HST* photometry in this region is unaffected. The influence of optical emission lines on the photometry was estimated using the ratio of line EWs taken from Fischer et al. (1998) to *HST* filter widths. The H$\alpha$ contribution to the *I* image is estimated at $\approx 3\%$ using the scaled H$\beta$ line (see Section 3.4.1), and the combined H$\beta$, [O II], and [O III] contribution to the *V* image is $\approx 7\%$. The low percentages imply the stellar continuum should be well-represented.

RBS 797 was imaged in the far-UV (FUV; 1344–1786 Å) and near-UV (NUV; 1771–2831 Å) with *GALEX*, and the near-UV with the *XMM-Newton*/Optical-Monitor (*XOM*) using filters UVW1 (2410–3565 Å) and UVM2 (1970–2675 Å). The *GALEX* pipeline produced images were used for analysis, and the *XOM* data was processed using SAS version 8.0.1. RBS 797 is detected in all but the UVM2 observation as an unresolved source co-spatial with the optical and X-ray BCG emission. The individual filter fluxes are $f_{\rm FUV} = 19.2 \pm 4.8$ $\mu$Jy, $f_{\rm NUV} = 5.9 \pm 2.1$ $\mu$Jy, $f_{\rm UVW1} = 14.6 \pm 4.6$ $\mu$Jy and $f_{\rm UVM2} < 117$ $\mu$Jy, all of which lie above the nuclear power-law emission we attribute to unresolved jets (see Section 3.5 and Figure 9).

A radial $(V - I)$ color profile of the central $2''$ ($\approx 10$ kpc) was extracted from the *HST* images and fitted with the function $\Delta(V - I)\log r + b$, where $\Delta(V - I)$ [mag dex$^{-1}$] is the color gradient, $r$ is radius, and $b$ [mag] is a normalization. The best-fit parameters are $\Delta(V - I) = -0.20 \pm 0.02$ and $b = 1.1 \pm 0.01$ for $\chi^2() = 0.009(21)$, revealing a flat, red color profile consistent with other BCGs that do not have strong nuclear star formation (*e.g.* Rafferty et al. 2006). Star formation rates were calculated from the UV fluxes using the relations of Kennicutt (1998), Moustakas et al. (2006), and Salim et al. (2007), which yield rates in the range 1–10 M$_\odot$ yr$^{-1}$ (see Table 4), relatively small values for what would be considered a strong cool core cluster. These estimates are likely upper limits since the blue *GALEX* color signals some AGN contamination (Agüeros et al. 2005), and sources of significant uncertainties have been neglected (*e.g.* Kennicutt 1992; Kewley et al. 2004; Hicks & Mushotzky 2005; Gilbank et al. 2010).

Taken together, the flat color profile and low star formation rate suggest any star formation may not be smoothly distributed in the halo but confined to compact regions like the bright substructures seen in the *HST* images. To better reveal the BCG substructure, residual galaxy images were constructed by first fitting the *HST* *V* and *I* isophotes with ellipses using the IRAF tool ELLIPSE. Stars and other contaminating sources were rejected using a combination of $3\sigma$ clipping and by-eye masking. The ellipse centers were fixed at the galaxy centroid, and ellipticity and position angle were fixed at $0.25 \pm 0.02$ and $-64° \pm 2°$, respectively – the mean values when they were free parameters. Galaxy light models were created using BMODEL in IRAF and subtracted from the corresponding parent image, leaving the residual images shown

in Figure 10. A color map was also generated by subtracting the fluxed *I* image from the fluxed *V* image.

The close alignment of the optical substructure with the nuclear AGN outflow clearly indicates the jets are interacting with the BCG halo. There also appears to be an in-falling galaxy northwest of the nucleus, possibly with a stripped tail (see Sun et al. 2007, for example). The numbered regions overlaid on the residual *V* image are the areas of the color map which have the largest color difference with surrounding galaxy light. Regions 1–5 are relatively the bluest with $m_{V-I} =$ –0.40, –0.30, –0.25, –0.22, and –0.20, respectively. Regions 6–8 are relatively the reddest with $m_{V-I} =$ +0.10, +0.15, and +0.18, respectively. Without spectroscopy, we can only speculate that the blue regions may be star formation sites, the red regions areas of heavy reddened by dust extinction, or both may be strong emission line regions.

Clusters like RBS 797 with a core entropy less than 30 keV cm$^2$ often host a BCG surrounded by extended H$\alpha$ nebulae (*e.g.* McDonald et al. 2010). Like these systems, the residual *I* image reveals what appear to be 8–10 kpc long "whiskers" surrounding the BCG (regions 9–11). It is interesting that blue regions 1 and 4 reside at the point where the southern jet appears to be encountering whiskers 9 and 10. It may be that the jet is interacting with gas in the whiskers and possibly driving star formation. If the AGN outflow is driving star formation then the estimated SFRs will be boosted above the putative rate, narrowing the difference between the AGN mass accretion and star formation rates and exacerbating the difficulty with cold-mode accretion (see Section 3.4).

## 4. CONCLUSIONS

We have presented results from a study of the AGN outburst in the galaxy cluster RBS 797. *CXO* observations have enabled us to constrain the energetics of the AGN outburst and analyze different powering mechanisms. We have shown the following:

1. In addition to the two obvious cavities near the cluster core, residual imaging reveals extensive substructure in the ICM (Figure 3) which has nebulous correlation with coincident radio emission. This leads us to speculate that the cavity system may be much larger and more complex than the present data allows us to constrain.

2. We find that the two central cavities have surface brightness decrements that are inconsistent with the cavities being spheres whose centers lie in a plane perpendicular to our line of sight which passes through the central AGN. Motivated by the decrement analysis, we propose that the cavities are either highly-elongated structures in the plane of the sky, or result from the superposition of much larger structures lying along our line of sight.

3. Using the cavity decrements as a constraint, we estimate the total AGN outburst energy at $3-6 \times 10^{60}$ erg with a total power output of $3-6 \times 10^{45}$ erg s$^{-1}$. There is the possibility that the cavities are larger than we have assumed and consider the energetics estimates as lower limits. The thick, bright rims surrounding the cavities may also be signaling the presence of shocks, which would further boost the AGN energy output.

4. The AGN energetics demand that accretion of cold or hot gas operate with unrealistic efficiency if mass accretion alone powered the outburst. We specifically show

that Bondi accretion is an unattractive solution, and instead suggest that the outburst may have been powered by tapping the energy stored in a maximally spinning SMBH. We show that hybrid spin models can achieve the calculated jet powers with accretion rates below 0.3 $M_\odot$ yr$^{-1}$.

5. Using primarily *HST* optical images, we present the discover of substructure in the BCG stellar halo which clearly indicates the AGN is interacting with the host galaxy. While we are unable to determine if any regions of interest host star formation or line emission, the convergence of what appear to be extended optical filaments, bluish knots of emission, and the tip of one jet suggest may be AGN driven star formation. We interpret the paucity of star formation indicators as a further sign that cold-mode accretion is not a favorable method of powering the AGN outburst.

## REFERENCES

Agüeros, M. A., Ivezić, Ž., Covey, K. R., Obrić, M., Hao, L., Walkowicz, L. M., West, A. A., Vanden Berk, D. E., Lupton, R. H., Knapp, G.R., Gunn, J. E., Richards, G. T., Bochanski, Jr., J., Brooks, A.,Claire, M., Haggard, D., Kaib, N., Kimball, A., Gogarten, S. M., Seth, A., & Solontoi, M. 2005, AJ, 130, 1022 6

Allen, S. W., Dunn, R. J. H., Fabian, A. C., Taylor, G. B., & Reynolds, C. S. 2006, MNRAS, 372, 21 1

Anders, E., & Grevesse, N. 1989, Geochim. Cosmochim. Acta, 53, 197 3

Arnaud, K. A. 1996, in Astronomical Society of the Pacific Conference Series, Vol. 101, Astronomical Data Analysis Software and Systems V, ed. G. H. Jacoby & J. Barnes, 17–+ 2

Begelman, M. C., Blandford, R. D., & Rees, M. J. 1984, Reviews of Modern Physics, 56, 255 1

Benson, A. J., & Babul, A. 2009, MNRAS, 397, 1302 1, 5

Bîrzan, L., McNamara, B. R., Nulsen, P. E. J., Carilli, C. L.,& Wise, M. W. 2008, ApJ, 686, 859 1, 2

Bîrzan, L., Rafferty, D. A., McNamara, B. R., Wise, M. W., & Nulsen, P. E. J. 2004, ApJ, 607, 800 1

Blandford, R. D., & Payne, D. G. 1982, MNRAS, 199, 883 5

Blandford, R. D., & Znajek, R. L. 1977, MNRAS, 179, 433 5

Bower, R. G., Benson, A. J., Malbon, R., Helly, J. C., Frenk, C. S., Baugh, C. M., Cole, S., & Lacey, C. G. 2006, MNRAS, 370, 645 1

Cavagnolo, K. W., Donahue, M., Voit, G. M., & Sun, M. 2008a, ApJ, 683, L107 1

—. 2008b, ApJ, 682, 821 3

—. 2009, ApJS, 182, 12 3

Crawford, C. S., Allen, S. W., Ebeling, H., Edge, A. C., & Fabian, A. C. 1999, MNRAS, 306, 857 4

Croton, D. J., Springel, V., White, S. D. M., De Lucia, G., Frenk, C. S., Gao, L., Jenkins, A., Kauffmann, G., Navarro, J. F., & Yoshida, N.2006, MNRAS, 365, 11 1

De Filippis, E., Schindler, S., & Castillo-Morales, A. 2002, arXiv e-prints: 0201349 1

Dunn, R. J. H., & Fabian, A. C. 2006, MNRAS, 373, 959 1

Edge, A. C. 2001, MNRAS, 328, 762 4

Ferrarese, L., & Merritt, D. 2000, ApJ, 539, L9 1, 4

Fischer, J.-U., Hasinger, G., Schwope, A. D., Brunner, H., Boller, T., Trümper, J., Voges, W., & Neizvestnyj, S. 1998, Astronomische Nachrichten, 319, 347 4, 6

Frank, J., King, A., & Raine, D. J. 2002, Accretion Power in Astrophysics: Third Edition, ed. Frank, J., King, A., & Raine, D. J. 4

Garofalo, D., Evans, D. A., & Sambruna, R. M. 2010, MNRAS, 820 5

Gebhardt, K., Bender, R., Bower, G., Dressler, A., Faber, S.M., Filippenko, A. V., Green, R., Grillmair, C., Ho, L. C., Kormendy, J., Lauer, T. R., Magorrian, J., Pinkney, J., Richstone, D., & Tremaine, S. 2000, ApJ, 539, L13 1

Gilbank, D. G., Baldry, I. K., Balogh, M. L., Glazebrook, K.,& Bower, R. G. 2010, MNRAS, 626 6

Gitti, M., Feretti, L., & Schindler, S. 2006, A&A, 448, 853 1, 2

Graham, A. W. 2007, MNRAS, 379, 711 4

Häring, N., & Rix, H. 2004, ApJ, 604, L89 4

Heavens, A. F., & Meisenheimer, K. 1987, MNRAS, 225, 335 5

Hicks, A. K., & Mushotzky, R. 2005, ApJ, 635, L9 6

Hughes, S. A., & Blandford, R. D. 2003, ApJ, 585, L101 1

Kalberla, P. M. W., Burton, W. B., Hartmann, D., Arnal, E. M.,Bajaja, E., Morras, R., & Pöppel, W. G. L. 2005, A&A, 440, 775 2

Kauffmann, G., & Haehnelt, M. 2000, MNRAS, 311, 576 1

Kennicutt, Jr., R. C. 1992, ApJ, 388, 310 6

—. 1998, ARA&A, 36, 189 6, 8

Kewley, L. J., Geller, M. J., & Jansen, R. A. 2004, AJ, 127, 2002 6

Kormendy, J., & Richstone, D. 1995, ARA&A, 33, 581 1, 4

Kriss, G. A., Cioffi, D. F., & Canizares, C. R. 1983, ApJ, 272, 439 3

Magorrian, J., Tremaine, S., Richstone, D., Bender, R., Bower, G., Dressler, A., Faber, S. M., Gebhardt, K., Green, R., Grillmair, C., Kormendy, J., & Lauer, T. 1998, AJ, 115, 2285 1, 4

McDonald, M., Veilleux, S., Rupke, D. S. N., & Mushotzky, R. 2010, ApJ, 721, 1262 6

McNamara, B. R., Kazemzadeh, F., Rafferty, D. A., Bîrzan, L, Nulsen, P. E. J., Kirkpatrick, C. C., & Wise, M. W. 2009, ApJ, 698, 594 1, 5

McNamara, B. R., & Nulsen, P. E. J. 2007, ARA&A, 45, 117 1

McNamara, B. R., Nulsen, P. E. J., Wise, M. W., Rafferty, D. A, Carilli, C., Sarazin, C. L., & Blanton, E. L. 2005, Nature, 433, 45 1

McNamara, B. R., Rohanizadegan, M., & Nulsen, P. E. J. 2010, arXiv e-prints: 1007.1227 1, 5

Meier, D. L. 1999, ApJ, 522, 753 5

—. 2001, ApJ, 548, L9 5

—. 2002, New Astronomy Review, 46, 247 1, 5

Mewe, R., Gronenschild, E. H. B. M., & van den Oord, G. H. J. 1985, A&AS, 62, 197 2

Moustakas, J., Kennicutt, Jr., R. C., & Tremonti, C. A. 2006,ApJ, 642, 775 4, 6, 8

Nemmen, R. S., Bower, R. G., Babul, A., & Storchi-Bergmann, T. 2007, MNRAS, 377, 1652 5

Nulsen, P. E. J., Hambrick, D. C., McNamara, B. R., Rafferty,D., Bîrzan, L., Wise, M. W., & David, L. P. 2005, ApJ, 625, L9 1

Pizzolato, F., & Soker, N. 2005, ApJ, 632, 821 1, 4

—. 2010, MNRAS, 408, 961 4

Quataert, E., & Narayan, R. 1999, ApJ, 520, 298 5

Rafferty, D. A., McNamara, B. R., & Nulsen, P. E. J. 2008, ApJ,687, 899 1

Rafferty, D. A., McNamara, B. R., Nulsen, P. E. J., & Wise, M. W. 2006, ApJ, 652, 216 1, 6

Reynolds, C. S., Garofalo, D., & Begelman, M. C. 2006, ApJ, 65l, 1023 5

Salim, S., Rich, R. M., Charlot, S., Brinchmann, J., Johnson, B. D., Schiminovich, D., Seibert, M., Mallery, R., Heckman, T. M.,Forster, K., Friedman, P. G., Martin, D. C., Morrissey, P., Neff, S. G., Small, T., Wyder, T. K., Bianchi, L., Donas, J., Lee, Y.-W., Madore, B. F., Milliard, B., Szalay, A. S., Welsh, B. Y., & Yi, S. K. 2007, ApJS, 173, 267 6, 8

Salomé, P., & Combes, F. 2003, A&A, 412, 657 4

Schindler, S., Castillo-Morales, A., De Filippis, E., Schwope, A., & Wambsganss, J. 2001, A&A, 376, L27 1, 2, 3

Schwope, A., Hasinger, G., Lehmann, I., Schwarz, R., Brunner, H., Neizvestny, S., Ugryumov, A., Balega, Y., Trümper, J., & Voges, W. 2000, Astronomische Nachrichten, 321, 1 4

Seaquist, E. R. 1993, Reports on Progress in Physics, 56, 1145 2

Sijacki, D., Springel, V., di Matteo, T., & Hernquist, L. 2007, MNRAS, 380, 877 1

Sikora, M., Stawarz, Ł., & Lasota, J. 2007, ApJ, 658, 815 1

Silk, J., & Rees, M. J. 1998, A&A, 331, L1 1

Sun, M., Donahue, M., & Voit, G. M. 2007, ApJ, 671, 190 6

Tremaine, S., Gebhardt, K., Bender, R., Bower, G., Dressler, A., Faber, S. M., Filippenko, A. V., Green, R., Grillmair, C., Ho, L. C.,Kormendy, J., Lauer, T. R., Magorrian, J., Pinkney, J., & Richstone, D.2002, ApJ, 574, 740 1, 4

Vikhlinin, A., Markevitch, M., Murray, S. S., Jones, C., Forman, W., & Van Speybroeck, L. 2005, ApJ, 628, 655 3

Wise, M. W., McNamara, B. R., Nulsen, P. E. J., Houck, J. C., & David, L. P. 2007, ApJ, 659, 1153 1, 3

**Table 1**
Cavity Properties.

| Config. (1) | ID (2) | $a$ kpc (3) | $b$ kpc (4) | $r_{los}$ kpc (5) | $D$ kpc (6) | $t_{sonic}$ Myr (7) | $t_{buoy}$ Myr (8) | $t_{refill}$ Myr (9) | $E_{cav}$ $10^{60}$ erg (10) | $P_{cav}$ $10^{45}$ erg s$^{-1}$ (11) |
|---|---|---|---|---|---|---|---|---|---|---|
| 1 | E1 | $17.3\pm1.7$ | $10.7\pm1.1$ | $13.6\pm2.4$ | $23.2\pm2.3$ | $20.1\pm3.1$ | $28.1\pm4.4$ | $70.3\pm9.9$ | $1.51\pm0.35$ | $1.70\pm0.48$ |
| 1a | $\cdots$ | $\cdots$ | $\cdots$ | $23.4\pm2.3$ | $\cdots$ | $\cdots$ | $\cdots$ | $76.9\pm10.9$ | $2.59\pm0.61$ | $2.92\pm0.83$ |
| 1 | W1 | $\cdots$ | $\cdots$ | $13.6\pm1.9$ | $25.9\pm2.5$ | $20.3\pm4.1$ | $33.3\pm5.3$ | $74.4\pm10.5$ | $1.72\pm0.47$ | $1.64\pm0.52$ |
| 1a | $\cdots$ | $\cdots$ | $\cdots$ | $26.0\pm2.6$ | $\cdots$ | $\cdots$ | $\cdots$ | $82.8\pm11.7$ | $3.29\pm0.89$ | $3.13\pm0.99$ |

Note. — Col. (1) Cavity configuration; Col. (2) Cavity identification; Col. (3) Semi-major axis; Col. (4) Semi-minor axis; Col. (5) Line-of-sight cavity radius; Col. (6) Distance from central AGN; Col. (7) Sound speed age; Col. (8) Buoyancy age; Col. (9) Refill age; Col. (10) Cavity energy; Col. (11) Cavity power using $t_{buoy}$.

**Table 2**
Energetic and Mass Accretion Totals.

| Row | Param. | Units | Config-1 | Config-1a |
|---|---|---|---|---|
| (1) | $E_{cav}$ | $10^{60}$ erg | $3.23\pm1.16$ | $5.88\pm2.11$ |
| (2) | $P_{cav}$ | $10^{45}$ erg s$^{-1}$ | $3.34\pm1.41$ | $6.05\pm2.56$ |
| (3) | $M_{acc}$ | $10^7$ M$_\odot$ | $1.81\pm0.65$ | $3.29\pm1.18$ |
| (4) | $\dot{M}_{acc}$ | M$_\odot$ yr$^{-1}$ | $0.59\pm0.25$ | $1.07\pm0.45$ |
| (5) | $\Delta M_{BH}$ | $10^7$ M$_\odot$ | $1.63\pm0.59$ | $2.96\pm1.06$ |
| (6) | $\dot{M}_{BH}$ | M$_\odot$ yr$^{-1}$ | $0.53\pm0.23$ | $0.96\pm0.41$ |
| (7) | $\dot{m}_E$ | – | 0.02 | 0.03 |
| (8) | $\dot{m}_B$ | – | 2130 | 3860 |

Note. — Row (1) Cavity energy; Row (2) Cavity power; Row (3) Mass accreted; Row (4) Mass accretion rate; Row (5) Black hole mass increase; Row (6) Black hole mass growth rate; Row (7) Eddington ratio; Row (8) Bondi ratio.

**Table 3**
AGN Spectral Models.

| Absorber (1) | $N_{H,abs}$ $10^{22}$ cm$^{-2}$ (2) | $\Gamma_{pl}$ (3) | $\eta_{pl}$ $10^{-5}$† (4) | $E_{ga}$ keV (5) | $\sigma_{ga}$ eV (6) | $\eta_{ga}$ $10^{-6}$‡ (7) | Param. (8) | $L_{0.6-7.0}$ $10^{44}$ erg s$^{-1}$ (9) | $L_{bol}$ $10^{44}$ erg s$^{-1}$ (10) | $\chi^2$ (11) | DOF (12) | Goodness (13) |
|---|---|---|---|---|---|---|---|---|---|---|---|---|
| None | $\cdots$ | $0.1^{+0.3}_{-0.3}$ | $0.3^{+0.1}_{-0.1}$ | [2.4, 3.4] | [63, 119] | [8.4, 14.9] | $\cdots$ | $0.69^{+0.11}_{-0.22}$ | $49.9^{+18.1}_{-19.0}$ | 1.88 | 61 | 56% |
| Neutral$^a$ | $4.2^{+1.9}_{-1.3}$ | $1.5^{+0.4}_{-0.3}$ | $6.6^{+8.1}_{-3.6}$ | [1.8, 3.0] | [3.1, 5.8] | [0.6, 1.8] | 0.354 | $0.68^{+0.12}_{-0.24}$ | $5.65^{+2.11}_{-2.50}$ | 1.17 | 60 | 29% |
| Warm$^b$ | $3.3^{+1.4}_{-1.6}$ | $1.9^{+0.2}_{-0.2}$ | $16.2^{+0.4}_{-0.5}$ | [1.8, 2.9] | [5.7, 4.4] | [0.9, 1.5] | $0.97^{+0.03}_{-0.03}$ | $0.70^{+0.18}_{-0.26}$ | $3.46^{+1.10}_{-0.95}$ | 1.01 | 59 | 13% |
| Power-law$^c$ | 0.5–7.5 | $2.1^{+0.5}_{-0.3}$ | $22.1^{+2.7}_{-1.1}$ | [1.8, 3.0] | [5.4, 3.5] | [0.9, 1.4] | $0.63^{+0.34}_{-0.31}$ | $0.71^{+1.48}_{-1.32}$ | $2.21^{+0.45}_{-0.30}$ | 1.00 | 58 | < 1% |

Note. — For all models, $N_{H,Gal} = 2.28 \times 10^{20}$ cm$^{-2}$. Col. (1) XSPEC absorber models: $a$ is ZWABS, $b$ is PCFABS, $c$ is PWAB; Col. (2) Absorbing column density; Col. (3) Power-law index; Col. (4) Power-law normalization with units (†) photons keV$^{-1}$ cm$^{-2}$ s$^{-1}$ at 1 keV; Col. (5) Gaussian central energies; Col. (6) Gaussian widths; Col. (7) Gaussian normalizations with units (‡) photons cm$^{-2}$ s$^{-1}$; Col. (8) Model-dependent parameter: absorber redshift for ZWABS, absorber covering fraction for PCFABS, absorber power law index of covering fraction for PWAB; Col. (9) Model 0.6-7.0 keV luminosity; Col. (10) Bolometric (0.01-100.0 keV) luminosity of model; Col. (11) Reduced $\chi^2$ of best-fit model; Col. (12) Model degrees of freedom; Col. (13) Percent of 10,000 Monte Carlo realizations with $\chi^2$ less than best-fit $\chi^2$.

**Table 4**
BCG Star Formation Rates.

| Source (1) | ID (2) | $\xi$ [Ref.] (M$_\odot$ yr$^{-1}$)/(erg s$^{-1}$ Hz$^{-1}$) (3) | $L$ erg s$^{-1}$ Hz$^{-1}$ (4) | $\psi$ M$_\odot$ yr$^{-1}$ (5) |
|---|---|---|---|---|
| *GALEX* | NUV | $1.4 \times 10^{-28}$ [2] | $2.5\ (\pm0.9) \times 10^{28}$ | $3.5\pm1.3$ |
| *XOM* | UVW1 | $1.1 \times 10^{-28}$ [3] | $6.2\ (\pm1.9) \times 10^{28}$ | $6.9\pm2.2$ |
| *GALEX* | FUV | $1.1 \times 10^{-28}$ [3] | $8.2\ (\pm2.0) \times 10^{28}$ | $9.0\pm2.3$ |
| *GALEX* | FUV | $1.4 \times 10^{-28}$ [2] | $8.2\ (\pm2.0) \times 10^{28}$ | $11\pm3$ |
| *XOM* | UVM2 | $1.1 \times 10^{-28}$ [3] | $< 5.0 \times 10^{29}$ | $< 55$ |

Note. — A dagger (†) indicates the removal of Hz$^{-1}$ from the units of $\xi$ & $L$. Col. (1) Source of measurement; Col. (2) Diagnostic identification; Col. (3) Conversion coefficient and references: [1] Moustakas et al. (2006), [2] Kennicutt (1998), [3] Salim et al. (2007); Col. (4) Luminosity; Col. (5) Star formation rate.
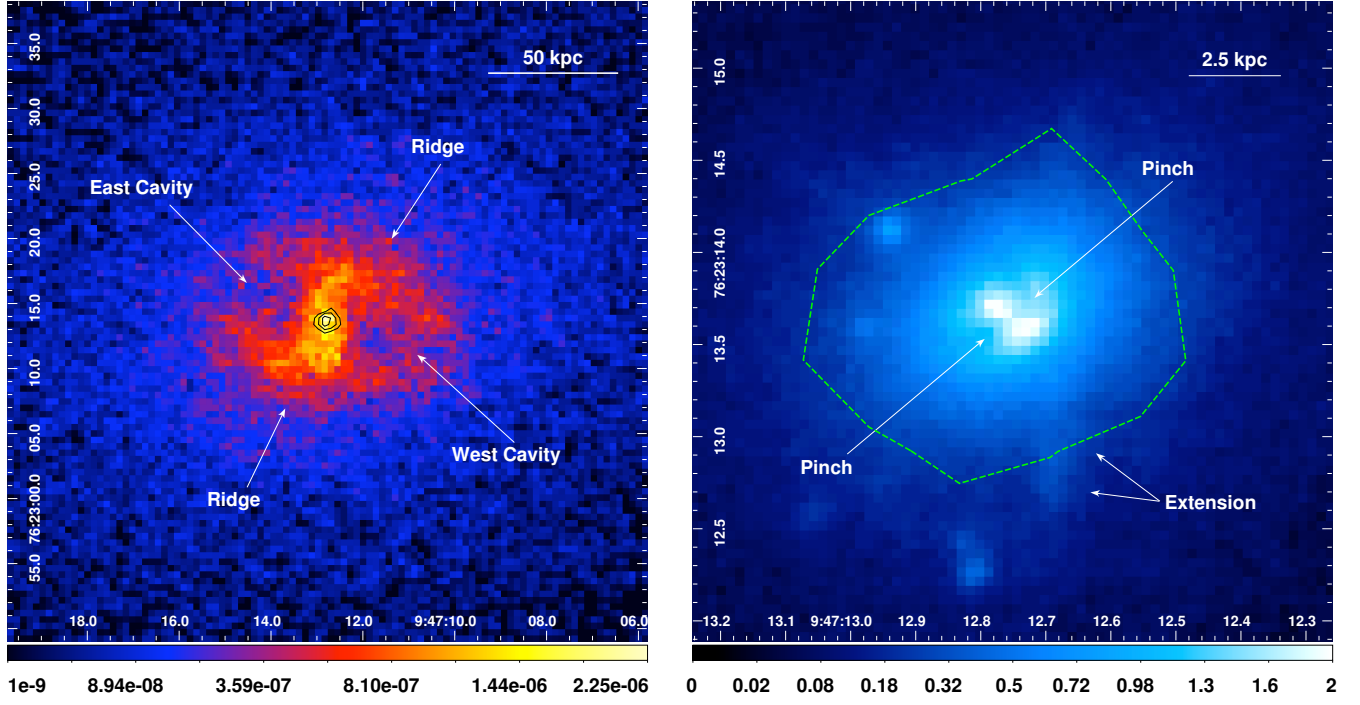
**Figure 1.** *Left:* Fluxed, unsmoothed 0.7–2.0 keV clean image of RBS 797 in units of ph cm$^{-2}$ s$^{-1}$ pix$^{-1}$. Image is $\approx$ 250 kpc on a side and coordinates are J2000 epoch. Black contours are 2.5–9.0 keV X-ray emission of the nuclear point source; the outer contour approximately traces the 90% enclosed energy fraction (EEF) of the *CXO* point spread function. *Right: HST I+V* image of the RBS 797 BCG with units e$^-$ s$^{-1}$. Green, dashed contour is approximately the *CXO* 90% EEF.
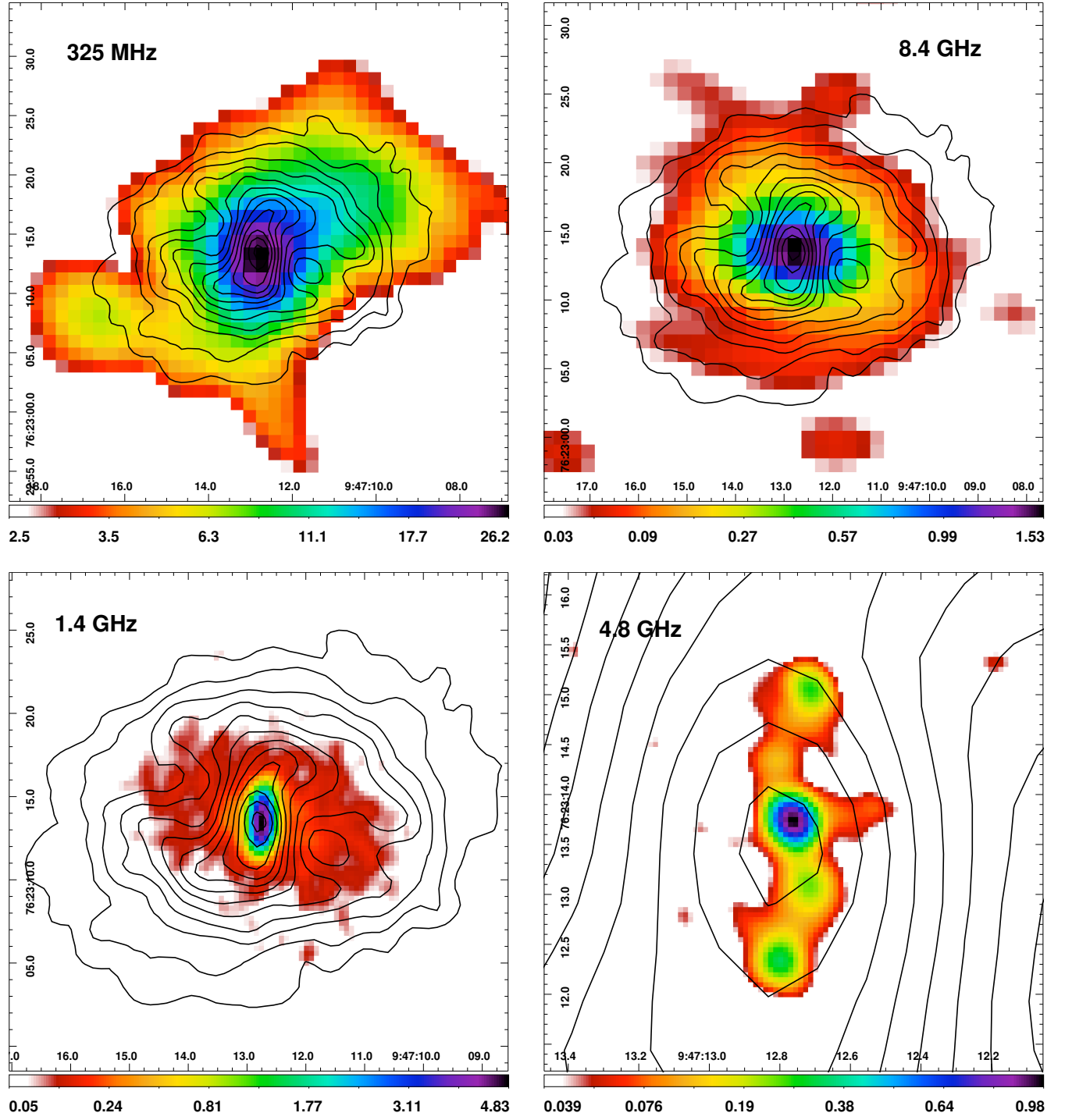
**Figure 2.** Radio images of RBS 797 overlaid with black contours tracing ICM X-ray emission. Images are in mJy beam$^{-1}$ with intensity beginning at $3\sigma_{\rm rms}$ and ending at the peak flux, and are arranged by decreasing size of the significant, projected radio structure. X-ray contours are from $2.3 \times 10^{-6}$ to $1.3 \times 10^{-7}$ ph cm$^{-2}$ s$^{-1}$ pix$^{-1}$ in 12 square-root steps. *Clockwise from top left:* 325 MHz *VLA* A-array, 8.4 GHz *VLA* D-array, 4.8 GHz *VLA* A-array, and 1.4 GHz *VLA* A-array.
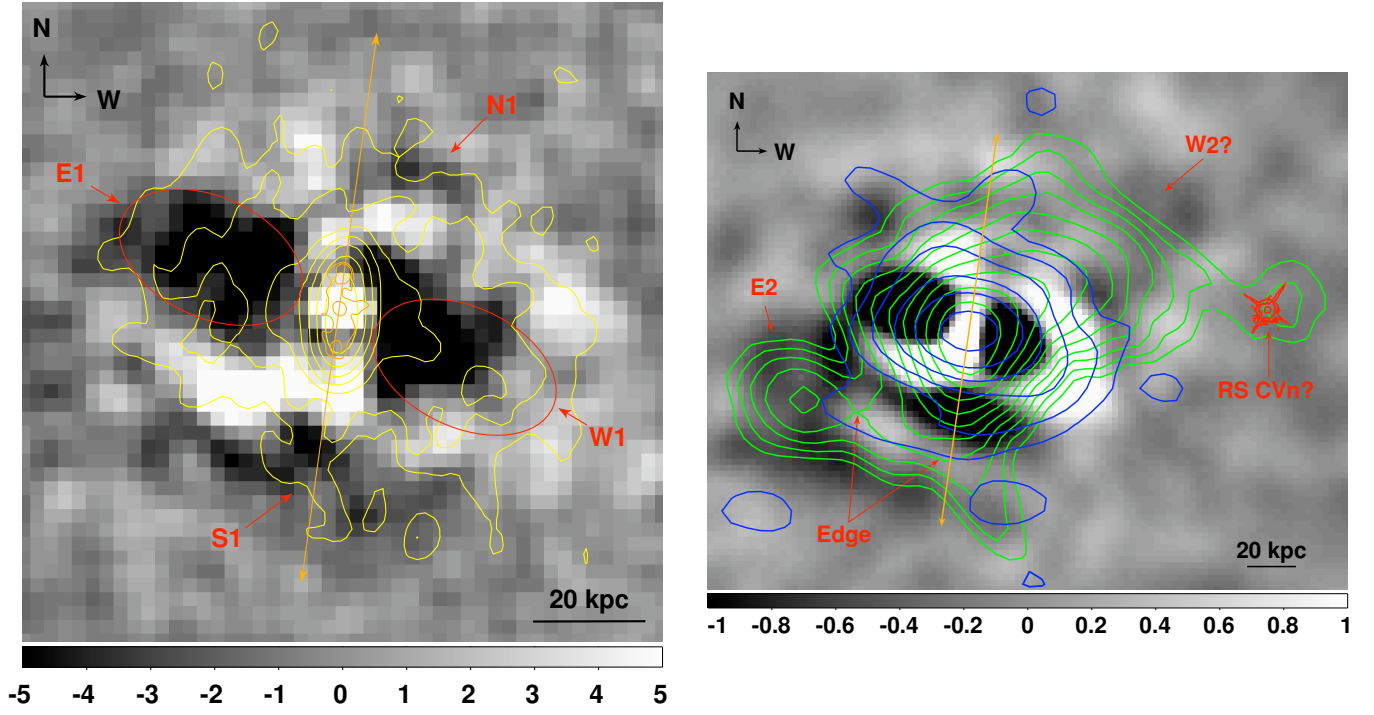
**Figure 3.** Red text point-out [regions] of interest discussed in Section 3.3. *Left:* Residual 0.3-10.0 keV X-ray image smoothed with 1″ Gaussian. Yellow contours are 1.4 GHz emission (*VLA* A-array), orange contours are 4.8 GHz emission (*VLA* A-array), orange vector is 4.8 GHz jet axis, and red ellipses outline definite cavities. *Bottom:* Residual 0.3-10.0 keV X-ray image smoothed with 3″ Gaussian. Green contours are 325 MHz emission (*VLA* A-array), blue contours are 8.4 GHz emission (*VLA* D-array), and orange vector is 4.8 GHz jet axis.

Cavagnolo et al.
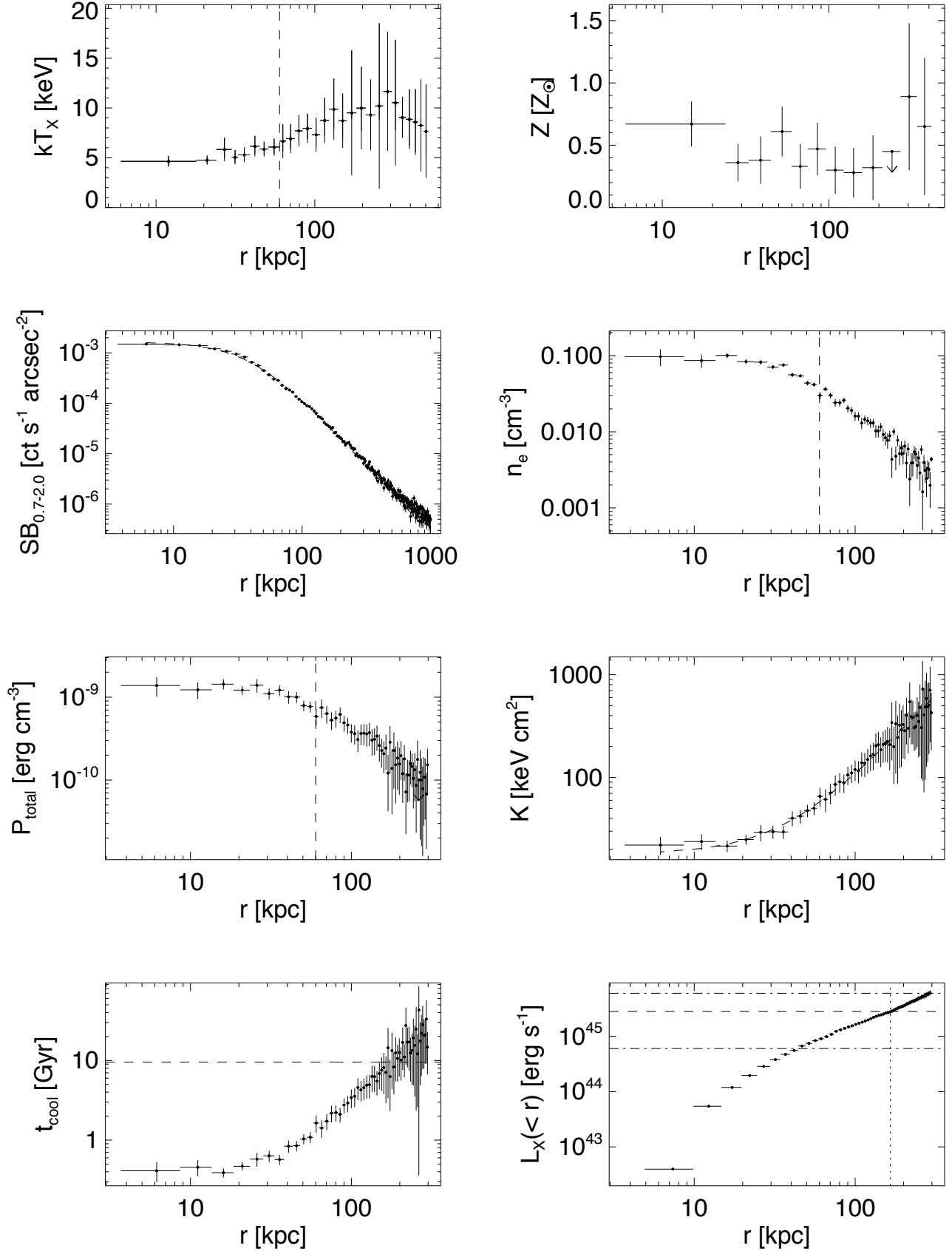


**Figure 4.** Gallery of radial ICM profiles. Vertical black dashed lines mark the approximate end-points of both cavities. Horizontal dashed line on cooling time profile marks age of the Universe at redshift of RBS 797. For X-ray luminosity profile, dashed line marks $L_{\rm cool}$, and dashed-dotted line marks $P_{\rm cav}$.
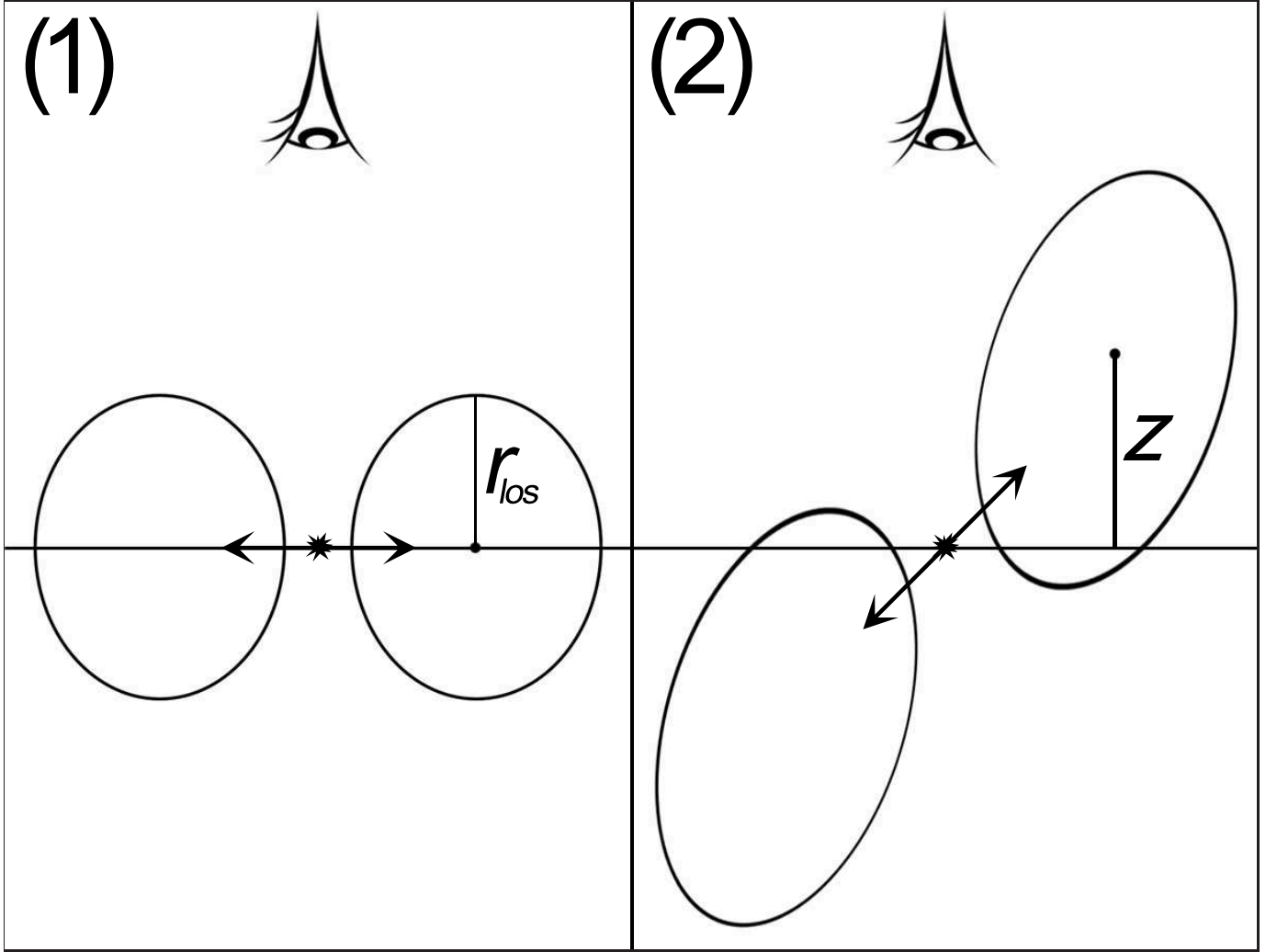
**Figure 5.** Cartoon of possible cavity configurations. Arrows denote direction of AGN outflow, ellipses outline cavities, $r_{los}$ is line-of-sight cavity depth, and $z$ is the height of a cavity's center above the plane of the sky. *Left:* Cavities which are symmetric about the plane of the sky, have $z = 0$, and are inflating perpendicular to the line-of-sight. *Right:* Cavities which are larger than left panel, have non-zero $z$, and are inflating along an axis close to our line-of-sight.
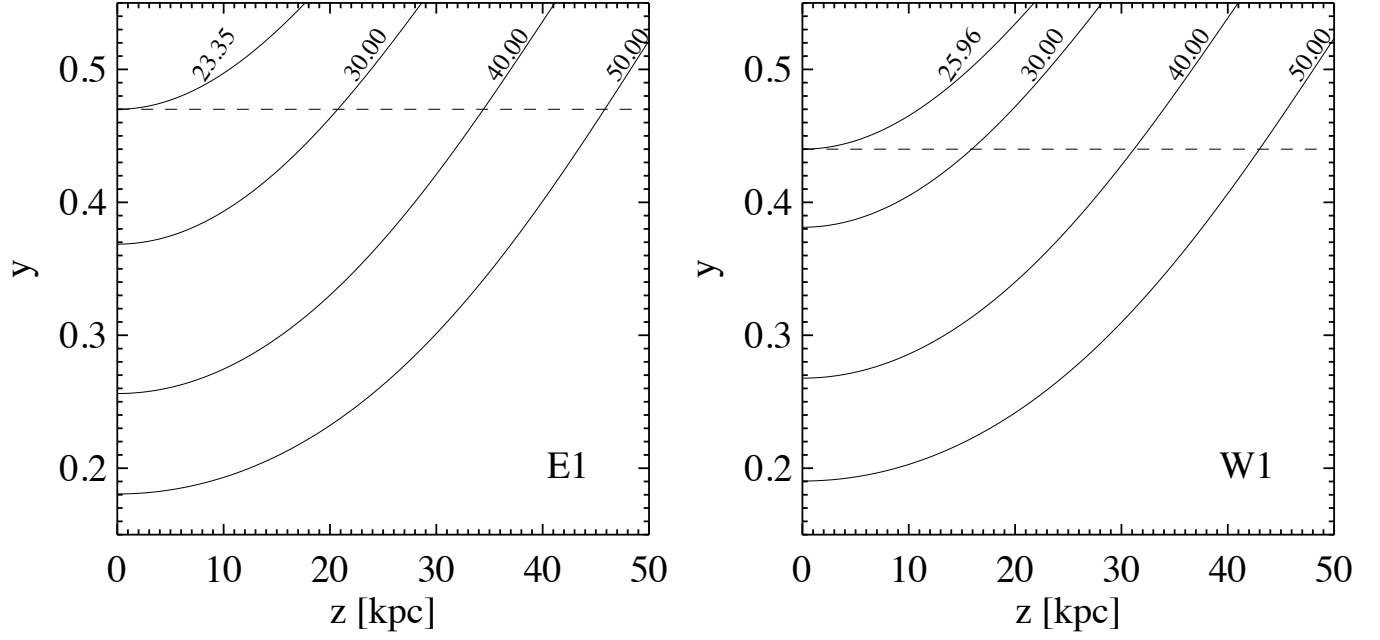
**Figure 6.** Surface brightness decrement as a function of height above the plane of the sky for a variety of cavity radii. Each curve is labeled with the corresponding $r_{\rm los}$. The curves furthest to the left are for the minimum $r_{\rm los}$ needed to reproduce $y_{\rm min}$, *i.e.* the case of $z = 0$, and the horizontal dashed line denotes the minimum decrement for each cavity. *Left* Cavity E1; *Right* Cavity W1.
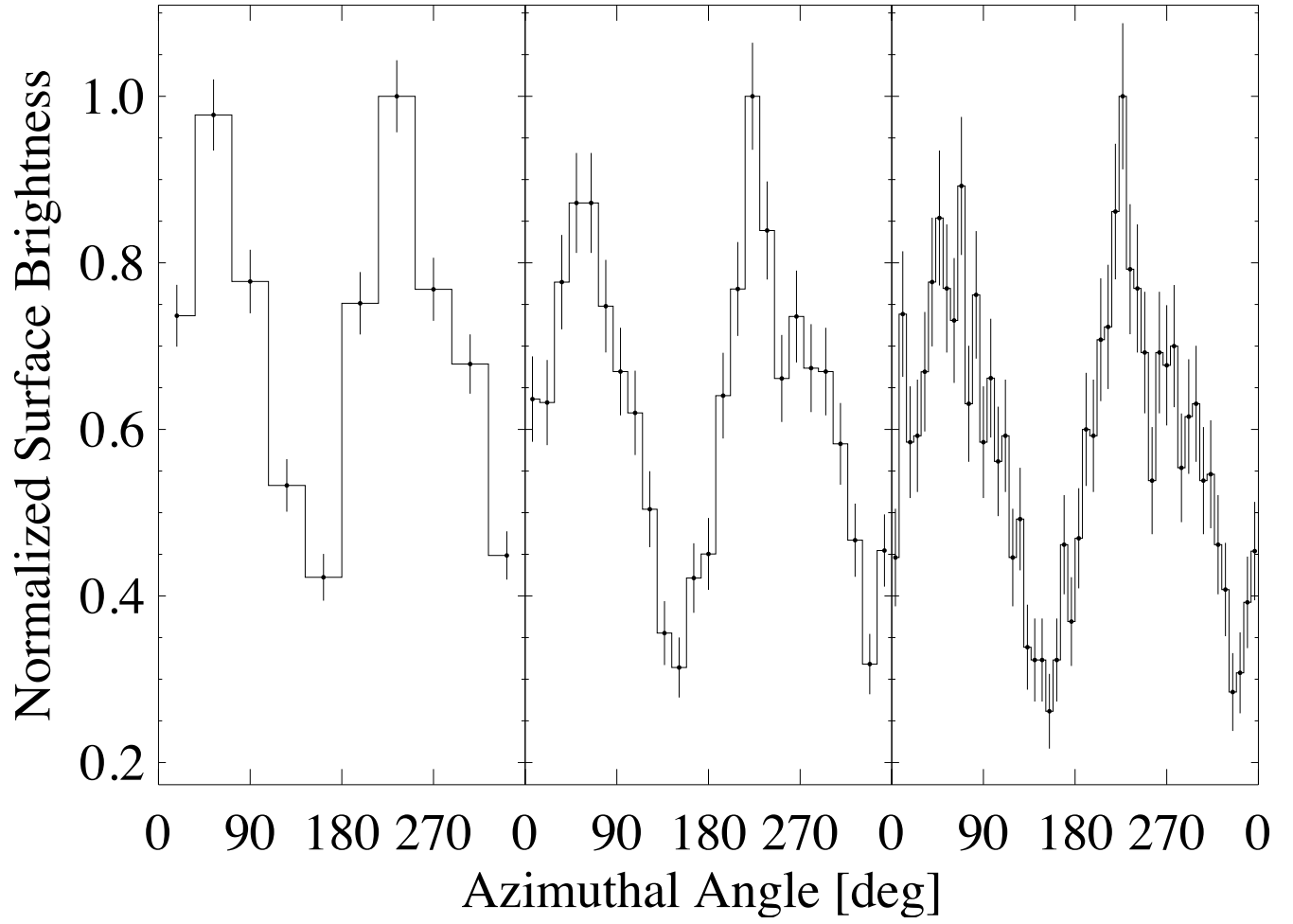
**Figure 7.** Histograms of normalized surface brightness variation in wedges of a 2.5″ wide annulus centered on the X-ray peak and passing through the cavity midpoints. *Left:* 36° wedges; *Middle:* 14.4° wedges; *Right:* 7.2° wedges. The depth of the cavities and prominence of the rims can be clearly seen in this plot.
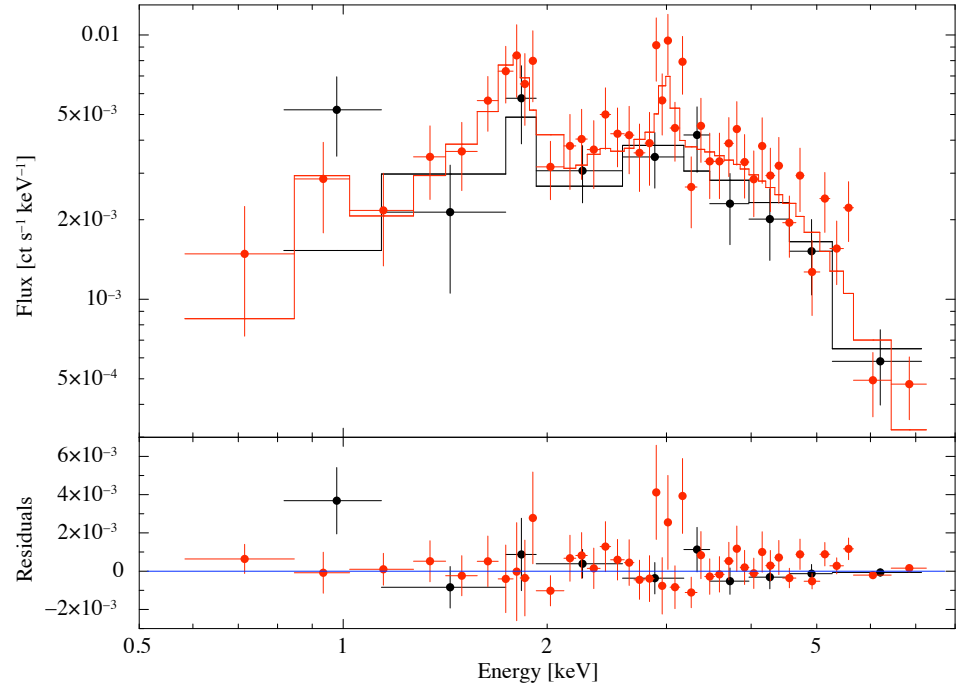
**Figure 8.** X-ray spectrum of nuclear point source. Black denotes year 2000 *CXO* data (points) and best-fit model (line), and red denotes year 2007 *CXO* data (points) and best-fit model (line). The residuals of the fit for both datasets are given below.
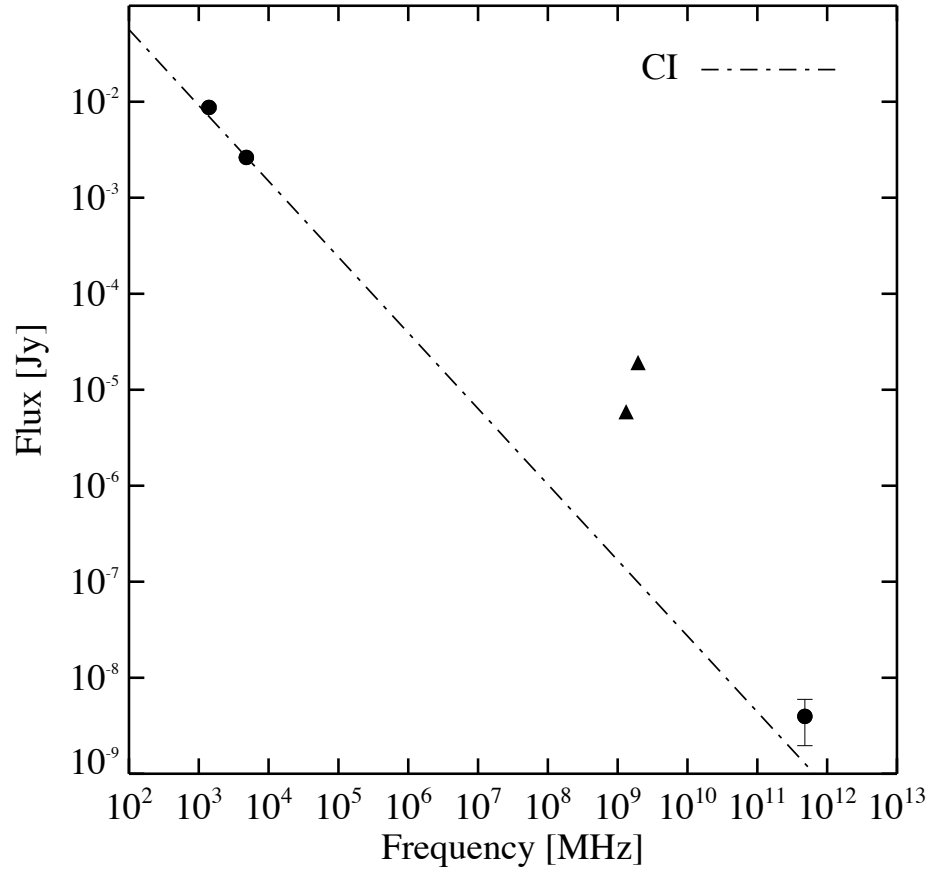
**Figure 9.** Best-fit continuous injection (CI) synchrotron model to the nuclear 1.4 GHz, 4.8 GHz, and 7.0 keV X-ray emission. The two triangles are *GALEX* UV fluxes showing the emission is boosted above the power-law atributable to the nucleus.
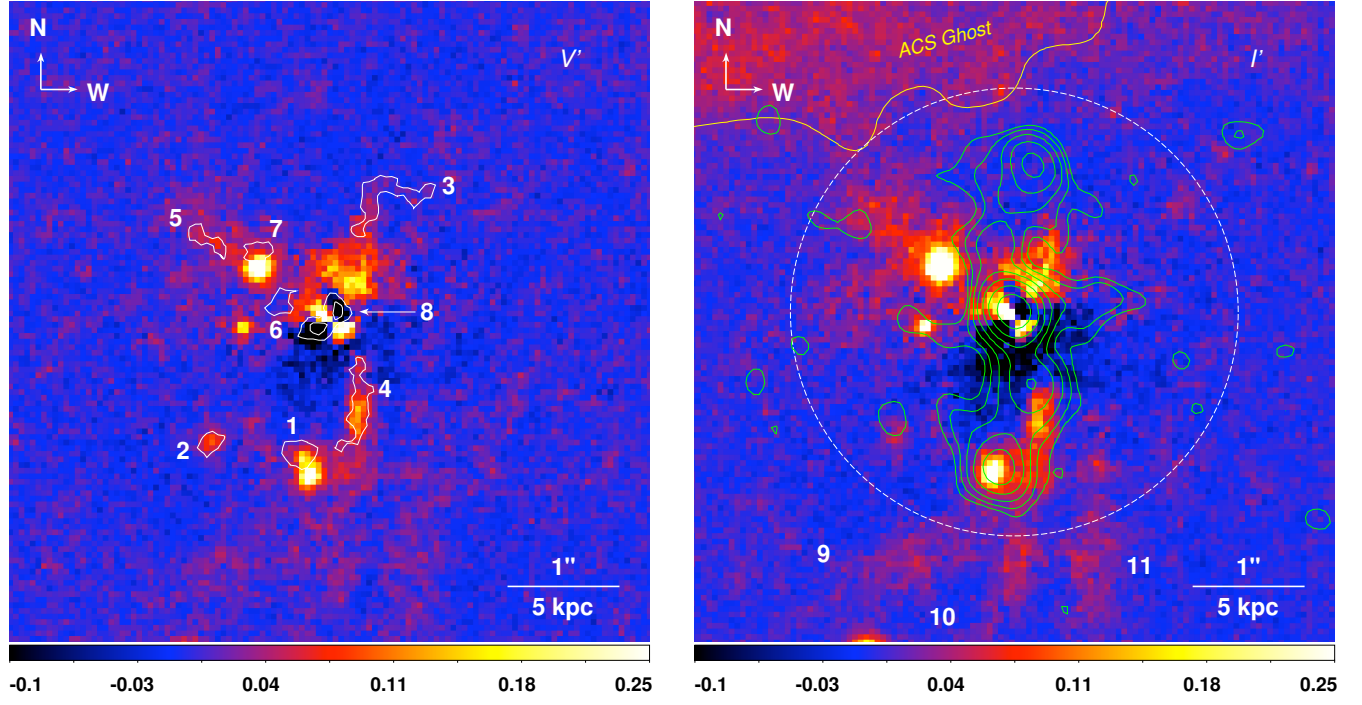
**Figure 10.** *Left* Residual *HST V* image. White regions (numbered 1–8) are areas with greatest color difference with RBS 797 halo. *Right* Residual *HST I* image. Green contours are 4.8 GHz radio emission, white dashed circle has radius 2″, edge of ACS ghost is show in yellow, and southern whiskers are numbered 9–11.